LASER & PHOTONICS REVIEWS
www.lpr-journal.org

Ferroelectric Polarization Enhanced Performance and Broadband Photodetector for Neural Network Recognition

Ruiqi Jiang, Yongfeng Jia, Fuxing Dai, Xuming Shi, Zhaotan Gao, Zhangxinyu Zhou, Hangrui Shi, Zhihao Wu, Yi Sun, Guoqiang Luo, Jin Wang, Fang Wang, Lin Wang, Jinzhong Zhang,* Zhigao Hu,* Junhao Chu, and Weida Hu*

The polarization electric field provided by ferroelectric materials can achieve precise control of the carrier concentration in van der Waals semiconductors, providing a more flexible, convenient, and efficient new approach for improving the performance and intelligent application of photodetectors. The UV-midinfrared photodetector with a sandwich structure of BP/MoS_2/CIPS, leverages the spontaneous polarization and Cu^+ ion migration within CIPS to modify the electric dipole moment at the interface between BP and MoS_2. This modification induces changes in the built-in electric field between BP and MoS_2, facilitating carrier separation and migration, thereby suppressing dark current and enhancing detectivity. Through gate voltage control, the device achieves an order-of-magnitude improvement in photocurrent, which demonstrates high specific blackbody detectivity, reaching up to 1.17 $\times 10^{10}$ cm in the infrared region. Furthermore, high-resolution images of letters are achieved by the BP/MoS_2/CIPS-based ferroelectric photodetectors. The devices achieve accurate image recognition by applying deep learning techniques. This work not only highlights the potential of CIPS-based device for high-sensitivity and broadband detection but also offers a new approach to neuromorphic computing applications.

1. Introduction

Ferroelectric materials are composed of crystal units with an inherent electric dipole moment. Below the Curie temperature (T_C), the electric dipoles can spontaneously align, forming a macroscopic polarization. Such an electric polarization state has non-volatile characteristics and can be reversibly regulated by an external electric field, providing a basis for the design of functional devices. Based on the integration technology of ferroelectric thin films and semiconductors, researchers have developed key components such as non-volatile memories, logic devices, and sensors. Among them, the ferroelectric gate dielectric field-effect transistor (FeFET) is regarded as one of the most promising architectures due to its non-destructive operation and non-volatile storage characteristics.[1,2] Traditional ferroelectric materials (ABO_3 perovskite oxides, HfO_2-based doped oxides,

R. Jiang, Z. Gao, J. Zhang, Z. Hu, J. Chu
Technical Center for Multifunctional Magneto-Optical Spectroscopy (Shanghai)
Engineering Research Center of Nanophotonics & Advanced Instrument (Ministry of Education)
Department of Physics, School of Physics and Electronic Science
East China Normal University
Shanghai 200241, China
E-mail: jzzhang@ee.ecnu.edu.cn; zghu@ee.ecnu.edu.cn

R. Jiang, Y. Jia, F. Dai, X. Shi, Z. Zhou, H. Shi, Z. Wu, J. Wang, F. Wang, L. Wang, J. Chu, W. Hu
State Key Laboratory of Infrared Physics
Shanghai Institute of Technical Physics
Chinese Academy of Sciences
Shanghai 200083, China
E-mail: wang_jin@tongji.edu.cn

X. Shi
Shanghai Research Institute for Intelligent Autonomous Systems
Tongji University
Shanghai 200092, China

Y. Sun, G. Luo
State Key Laboratory of Advanced Technology for Materials Synthesis and Processing
Wuhan University of Technology
Wuhan 430070, China

J. Wang
MOE Key Laboratory of Advanced Micro-Structure Materials
Shanghai Frontiers Science Center of Digital Optics
Institute of Precision Optical Engineering, and School of Physics Science and Engineer
Tongji University
Shanghai 200092, China

The ORCID identification number(s) for the author(s) of this article can be found under https://doi.org/10.1002/lpor.202500298

DOI: 10.1002/lpor.202500298

AlScN, and organic polymers like PVDF, etc.) have been preliminarily applied in 2D devices.[3] However, during the synthesis process, due to surface dangling bonds and lattice mismatch, their ultrathinning still faces significant challenges. In contrast, 2D layered ferroelectric materials (transition metal chalcogenides, group-IV metal chalcogenides, α-In_2Se_3, and $CuInP_2S_6$, etc.) exhibits advantages such as intrinsic ferroelectricity and a surface without dangling bonds, thanks to the weak van der Waals interlayer forces. This provides a new paradigm for atomically thin ferroelectric devices.[4,5] $CuInP_2S_6$ (CIPS) stands as one of the most emblematic layered ferroelectric materials within the category of Cu-containing transition metal sulfide (or selenide) phosphates.[6–10] 2D CIPS exhibits ferroelectric properties, which nearly reaches the theoretical limit, demonstrating significant potential for applications in 2D infrared detection combining with n-type MoS_2 (E_g ~ 1.2 eV) and narrow bandgap p-type BP (E_g ~ 0.3 eV).[11–15] The spontaneous ferroelectric polarization in CIPS arises from the displacement of Cu^+ ions from their central positions, which is driven by the second-order Jahn–Teller effect.[16–19] When the electric field reverses the ferroelectric domain, Cu^+ ions migrate in the vertical direction, leading to Cu^+ precipitation at the surface or interface.[20–23] Consequently, the polarization direction points out of the plane, making it easier to directly couple with the material at the interface. This coupling enables the regulation of the barrier height[24–26] and promotes the separation and migration of photogenerated carriers at the interface. Furthermore, the structural alterations resulting from Cu^+ ion diffusion in CIPS lead to a significant increase in photocurrent density,[27,28] specifically by one order of magnitude, due to the various band arrangements.

Convolutional neural networks (CNN) is a type of feedforward neural network that incorporates convolutional computation and a deep structure. It is one of the representative algorithms in deep learning.[29–31] By utilizing deep CNN, features can be automatically learned from original images. Classification and recognition can be carried out to achieve the goals of image recognition and object detection.[32] It has advantages such as automatic feature learning, strong extensibility, and efficient hardware acceleration. It is expected to address the prominent challenges faced by the traditional von Neumann computing platform in terms of information processing efficiency and functionality.[32–34] Moreover, CNN can efficiently extract features from complex images, significantly improving recognition accuracy and enabling precise identification in image recognition tasks.

This work presents the construction of a high-detectivity and broadband photodetector featuring a sandwich structure (BP/MoS_2/CIPS). When ferroelectric polarization arises, Cu^+ ions migrate to the interface between MoS_2 and CIPS, it results in a modification of the electric dipole moment and various built-in electric field between BP and MoS_2. The migration and diffusion of carriers can be controlled by manipulating the polarization direction of CIPS, resulting in a high specific blackbody detectivity of about 1.17×10^{10} cm · $Hz^{1/2}$ · W^{-1} in the infrared region. By implementing deep learning methods, the devices are able to accomplish highly accurate image recognition. This provides a novel theoretical exploration and device design approach for achieving high-sensitivity and UV-midinfrared photodetection at room temperature.

2. Results and Discussion

2.1. Structure of the BP/MoS_2/CIPS-based Ferroelectric Photodetector

Figures 1a and 1b are the structure schematic and optical microscope photograph of the BP/MoS_2/CIPS-based ferroelectric photodetector, respectively. The CIPS nansheet is placed above the bottom electrode, and MoS_2 and BP are transferred onto CIPS in sequence. Figure 1c shows the scanning transmission electron microscope (STEM) images and the energy dispersive X-ray spectrometry (EDS) elemental mapping of the device. It indicates that the interfaces of all layers are clear, flat and free of impurities. Furthermore, the EDS analysis of Cu, In, P, S and Mo elements indicate that all elements are uniformly distributed and there is no inter-diffusion among them. Noted that the distinct interfaces of BP/MoS_2 and MoS_2/CIPS are crucial for the photodetection performance. In addition, the crystalline and thickness of BP (~ 61 nm), MoS_2 (~ 14 nm), and CIPS (~ 145 nm) are conformed by Raman spectra and atomic force microscope (Figure S1, Supporting Information). In a further step, Figure 1d shows the phase and amplitude hysteresis loops of the ferroelectric CIPS measured by the piezoelectric force microscope (PFM). It suggests that the ferroelectric CIPS flakes have strong ferroelectric polarization due to the obvious 180-degree switching of phase signal and clear butterfly loops of amplitude.

2.2. Schematic Band Structure at Various Ferroelectric Polarization States

Figure 2a shows the schematic band structure of separated BP, MoS_2, and CIPS. The work function of MoS_2 and BP are ~4.6 and ~4.8 eV, respectively.[36,37] During the n-type MoS_2 contact with p-type BP, electrons are transferred from MoS_2 to BP, while holes are transferred from BP to MoS_2, which formes a heterojunction in equilibrium, as shown in Figure 2b. In order to accurately determine the junction barrier at the BP/MoS_2 heterostructure, the surface potential of the junction region between BP and MoS_2 at the three polarization states (fresh, up, and down) were measured using Kelvin probe force microscopy (KPFM) by applying a single pulsed gate voltage (2 V for the up sate and –2 V for the down state), as shown in (Figure 2c). In the fresh state, the surface potential difference between BP and MoS_2 is 0.223 eV (Figure 2d i). The band structure of the fresh state is shown in (Figure 2d ii). In the up state, Cu^+ within CIPS migrated to achieve a polarization of ferroelectric domains. A polarization electric field is continuously applied to MoS_2, which increases the electron concentration of MoS_2 and brings the bottom of conduction band closer to the Fermi level. Therefore, the surface potential difference increases to 0.252 eV (cf. Figure 2e i). The band structure of the BP/MoS_2 heterojunction shown in Figure 2e ii is constructed from that of the fresh state, which effectively blocks the dark current and improves the separation efficiency of photo-generated electron-hole pairs. On the contrary, the opposite situation occurs in the down state. Cu^+ within CIPS migrates under a negative gate voltage, thereby achieving reverse polarization of ferroelectric domains. The electric field generated by reverse polarization causes the Fermi level to shift downwards and the electron concentration of MoS_2 decreases. Therefore, the surface potential dif-

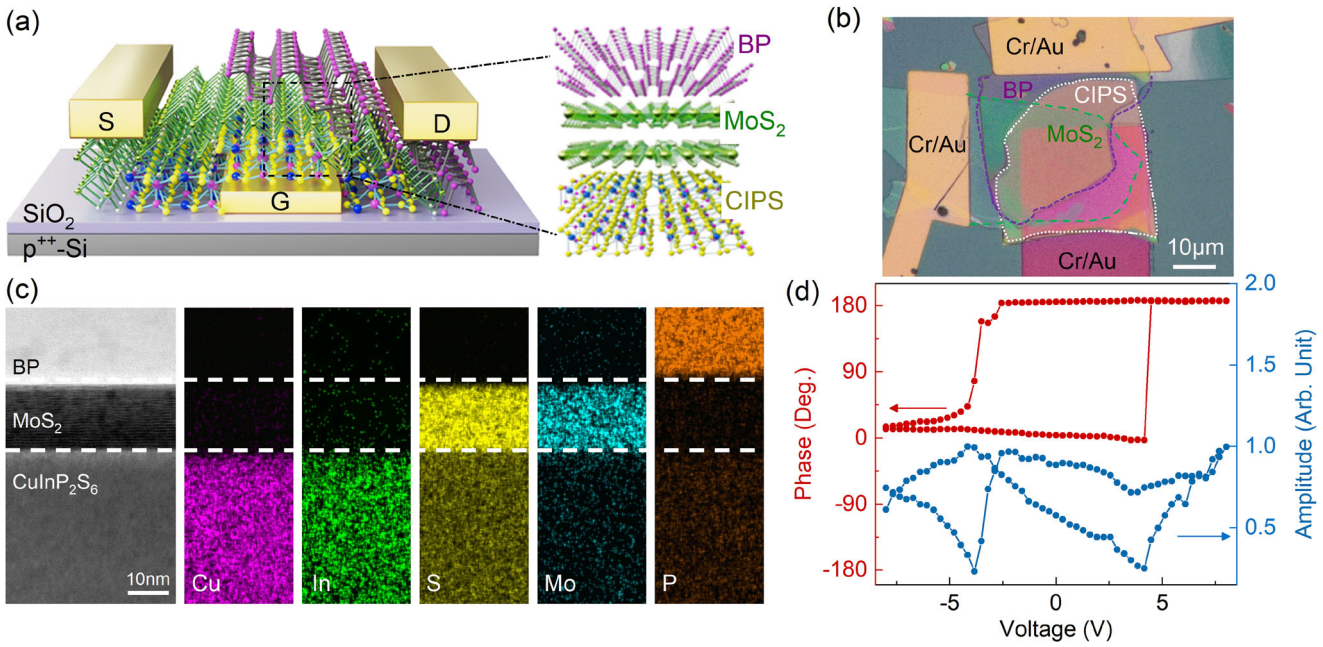

Figure 1. Characterizations of a BP/MoS_2/CIPS-based photodetector and the ferroelectricity of CIPS. a) Schematic diagram and b) optical microscope image of a BP/MoS_2/CIPS-based photodetector. c) Cross-sectional STEM image and EDS element mapping images of a BP/MoS_2/CIPS heterostructure. d) Out-of-plane amplitude and phase of a CIPS flake.

ference reduces to 0.211 eV (cf. Figure 2f i), which decreases the carrier transport efficiency (Figure 2f ii). Therefore, the polarization electric field of CIPS can regulate the Fermi level and carrier concentration of BP and MoS_2, improve the band structure and built-in electric field strength of BP/MoS_2 heterojunction, which will directionally suppress dark current, improve the separation and transport efficiency of photo generated carriers, and obtain a higher detectivity of the ferroelectric photodetectors.

2.3. Broadband Photoresponse of the BP/MoS_2/CIPS-based Detoctors

In **Figures** 3a and S2 (Supporting Information), the dark current at a up state and V_{DS} = −0.5 V decreases by one order of magnitude compared to that of the unpolarized state (fresh state), significantly improving the rectification ratio of the BP/MoS_2/CIPS-based photodetector. On the contrary, the dark current at a down state increases. To further verify the effect of ferroelectric polarization on the BP/MoS_2 heterojunction, photocurrent mapping tests under fresh and up states are performed at a wavelength of 2000 nm, as shown in Figure 3b. It reveals that the light response across the entire junction area is significantly enhanced since the carries in the channel are enhanced by the ferroelectric electric filed.[38,39] Furthermore, Figure 3c–e and Figures S3–S6 (Supporting Information) show the photovoltaic response under the illumination wavelengths of 295, 405, 520, 633, 1550, 2000, 2611, and 3622 nm, respectively. It indicates that the wavelength response of the BP/MoS_2/CIPS-based ferroelectric detector could cover the UV to mid-infrared (UV-MIR) region. As the laser power density increases, the photocurrent significantly increases. Noted that the photocurrent of the BP/MoS_2/CIPS detector as a function of laser intensity is measured at V_{DS} = 0 V. The self-powered photoresponse capability is attributed to the existence of a stable built-in electric field (depletion region) at the interface between n-type MoS_2 and p-type BP, which can facilitate the efficient separation and transfer of photogenerated electron-hole pairs even without an external power supply.

In Figure 3f and Figure S7 (Supporting Information), the current noise of the detector at up state is significantly lower than that in the fresh state. Generally, the noise in photodetector originate from 1/f noise, shot noise, and thermal noise. In this study, the device is measured at a modulation frequency of 317 Hz and the 1/f noise could be ignored. Shot noise and thermal noise contribute to the dark current. However, the dark current induced by shot noise is relatively low since the photodetector operated under zero bias. Therefore, thermal noise is the dominant source of the current noise for the BP/MoS_2 /CIPS-based detectors. Figure 3g and Figure S8 (Supporting Information) show the detector response speed under zero bias voltage and various laser wavelength illuminations. It indicates that there are short rise and decay times (τ_r = 35 μs, and τ_d = 60 μs) under 2000 nm illumination. Note that the BP/MoS_2/CIPS-based ferroelectric photodetectors illuminated at different laser wavelengths can still maintain a photoresponse close to the initial one without performance degradation after 1000 cycles of continuous photoresponse. It indicates that the ferroelectric photodetectors have excellent stability (Figure S9, Supporting Information). Furthermore, as a key performance parameter of photodetectors, specific detectivity D* is calculated by the formula: $D^* = (A\Delta f)^{1/2}/NEP = R\,(A\Delta f)^{1/2}/i_N$, where i_N is the noise current, R is the responsivity, A is the effective area of photodetectors, and Δf is the bandwidth.[13] At a blackbody temperature of 1200 K, the D* of the BP/MoS_2/CIPS-based photodetector is

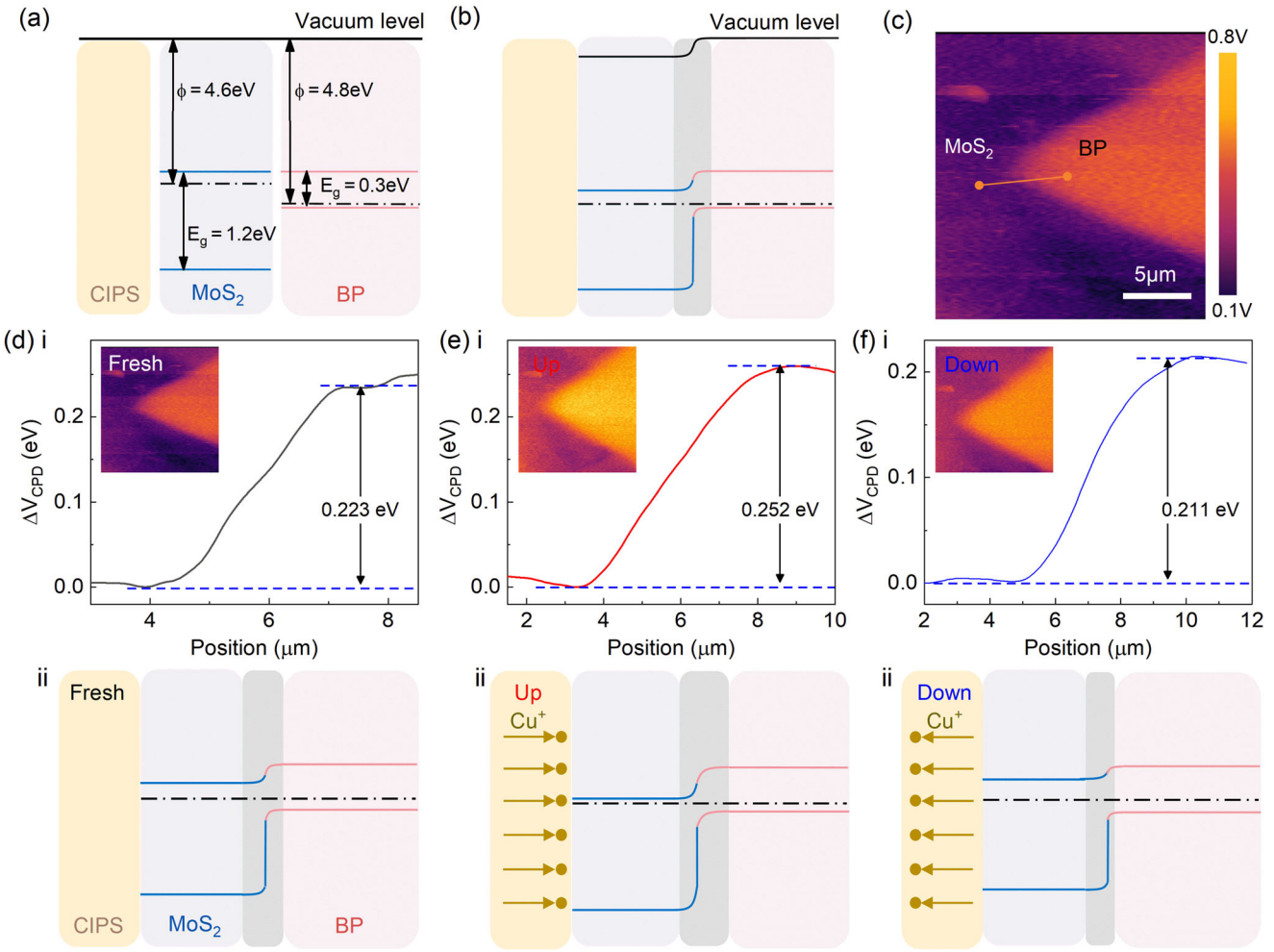

Figure 2. The BP/MoS_2/CIPS-based photodetector regulation principle of polarization electric field. Schematic band structure of a) separated and b) contacted CIPS, BP, and MoS_2. c) Surface potential image of the BP/MoS_2 heterostructure. Surface potential changes and the corresponding band structures in (d i, ii) fresh, (e i, ii) up, (f i, ii) down states, respectively.

measured as a function of wavelength, as shown in Figure 3h and Figure S10 (Supporting Information). Noted that the peak of blackbody D* in the infrared region reaches 1.17×10^{10} cm · $Hz^{1/2}$ · W^{-1}. The BP/MoS_2/CIPS-based ferroelectric photodetector exhibits a good detectivity performance compared with those of BP/MoS_2, PbSe, and HgCdTe photodetectors.[35,40–43] We have also compared the key parameters of the reported state-of-the-art photodetectors (Table S1, Supporting Information). Note that our photodetectors exhibit a higher detectivity under blackbody illumination compared with state-of-the-art photodetectors.

2.4. Image Recognition of the Photodetectors

An imaging system shown in **Figure** 4a is designed to evaluate the imaging performance of the BP/MoS_2/CIPS-based ferroelectric photodetectors. A steel plate with hollow patterns as an imaging target is placed in front of a laser source. A lens focuses the incident laser onto the photodetector. During the imaging process, the device is moved step-by-step both horizontally and vertically by a 2D motion platform controlled by a computer. The incident laser passes through the hollow plate irradiating the ferroelectric BP/MoS_2/CIPS-based photodetectors. Meanwhile, the position-resolved photocurrent is recorded in real-time by a source meter. Finally, the computer combines the photocurrent and position data to generate an image. Deep learning is a high-accuracy neuromorphic processing strategy which has substantially optimized computational performance for vast data. In this study, simulations are conducted on a CNN to recognize the letter images generated by scanning. The Extended Modified National Institute of Standards and Technology (EMNIST) dataset is adopted, which is a more challenging benchmark for classification tasks. The EMNIST dataset not only includes handwritten digits, but also handwritten English letters including uppercase and lowercase, providing a more comprehensive sample of handwritten characters. It provides rich samples and drives the development of deep learning techniques through various tasks. The CNN model shown in Figure 4b is developed based on the EMNIST dataset, which contains 814255 images of 62 categories. After the image is input, features are extracted by two convolution and pooling

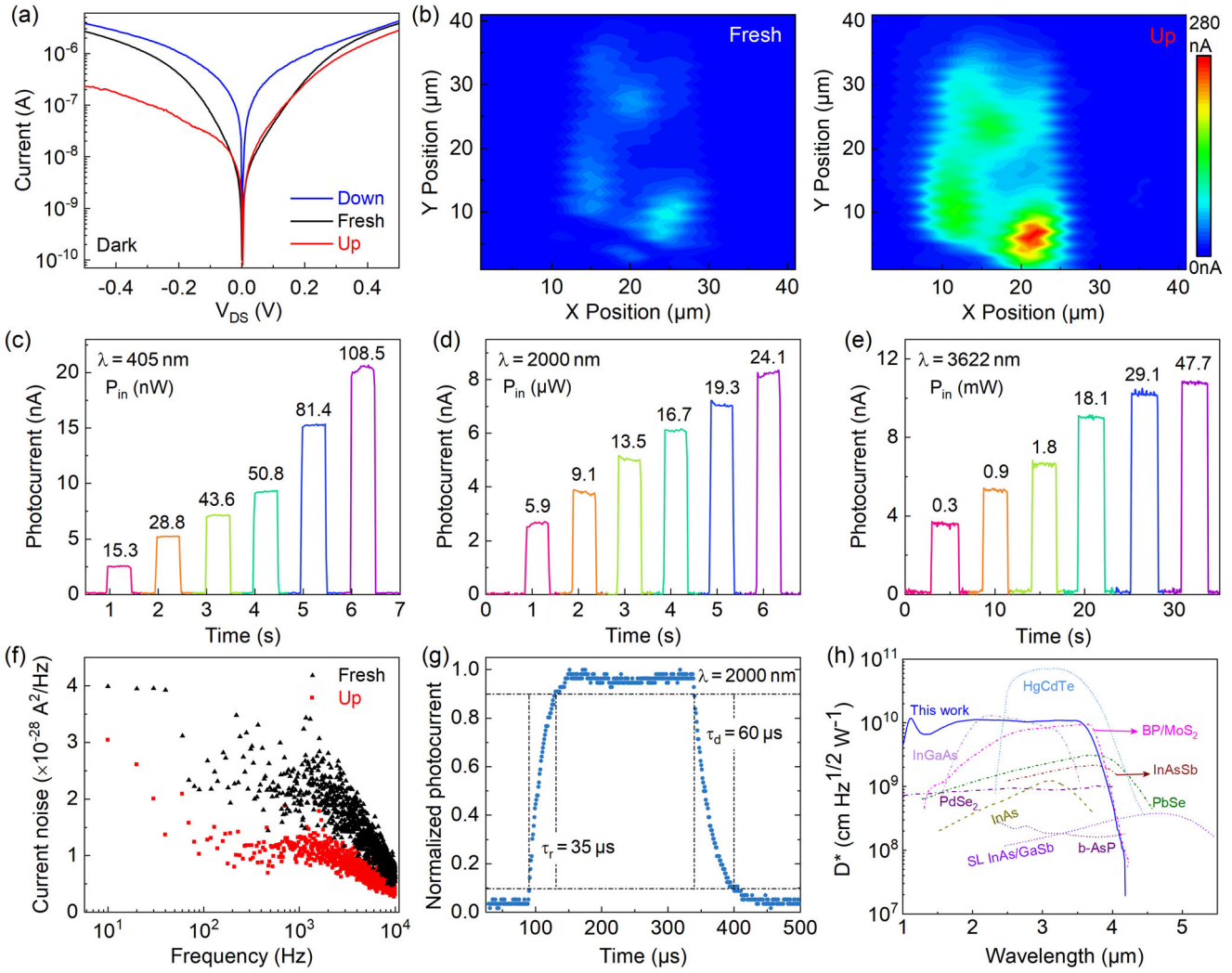

Figure 3. Photoresponse characterizations of a BP/MoS_2/CIPS-based photodetector. a) Output characteristic curves of the ferroelectric device in the fresh, up, and down states. b) Photocurrent distributed mapping of 2000 nm laser in the fresh and up states. Time-resolved photoresponse under illumination of c) 405 nm, d) 2000 nm, and e) 3622 nm. f) Current noise power density as a function of frequency in the fresh and up states. g) Normalized photocurrent for evaluating response speeds (rise/fall time) under 2000 nm. h) Comparison of photodetector detectivity as a function of wavelength.[35]

layers. Then the obtained feature map is flattened through a fully connected layer. Noted that when performing letter recognition in an image, the letter with the highest prediction probability is determined as the final result. Figure 4c presents the imaging results measured under V_{DS} = 0 V. High-resolution images of the English letters "ECNU" is achieved, demonstrating the powerful imaging ability of the ferroelectric BP/MoS_2/CIPS-based detector. Based on the images generated by device scanning, the performance of the detectors in the application for neuromorphic computing is evaluated. Figures 4d and 4e show that the accuracy of the training set approximates 88%, and the loss drops to as low as 0.31 after 90 training epochs. The difference between the training and validation sets is very small, which means that the proposed BP/MoS_2/CIPS-based detector has the potential for image recognition hardware. The actual imaging experiments on the device and the simulation of the CNN show that the photodetector can achieve high accuracy in pattern recognition tasks. The core of applying ferroelectric polarization in neuromorphic computing lies in its switchable spontaneous polarization and nonvolatile storage capabilities. These features, combined with the synergistic advantages of 2D materials, provide critical support for mimicking biological synaptic functions and enabling efficient in-memory computing. The polarization direction of ferroelectric materials can be switched by external electric fields, forming stable multistate resistive states with nonvolatile characteristics. This directly emulates the long-term potentiation (LTP) and long-term depression (LTD) of biological synapses, meeting the stringent requirements of neuromorphic systems for weight plasticity and long-term memory storage. Van der Waals heterostructures constructed with 2D materials (e.g., MoS_2, In_2Se_3) enable atomic-scale thickness devices. Such structures reduce the polarization switching voltage, enhance stability, and support low-power, high-density integration. Despite challenges in large-area synthesis of high-quality 2D ferroelectric materials and po-

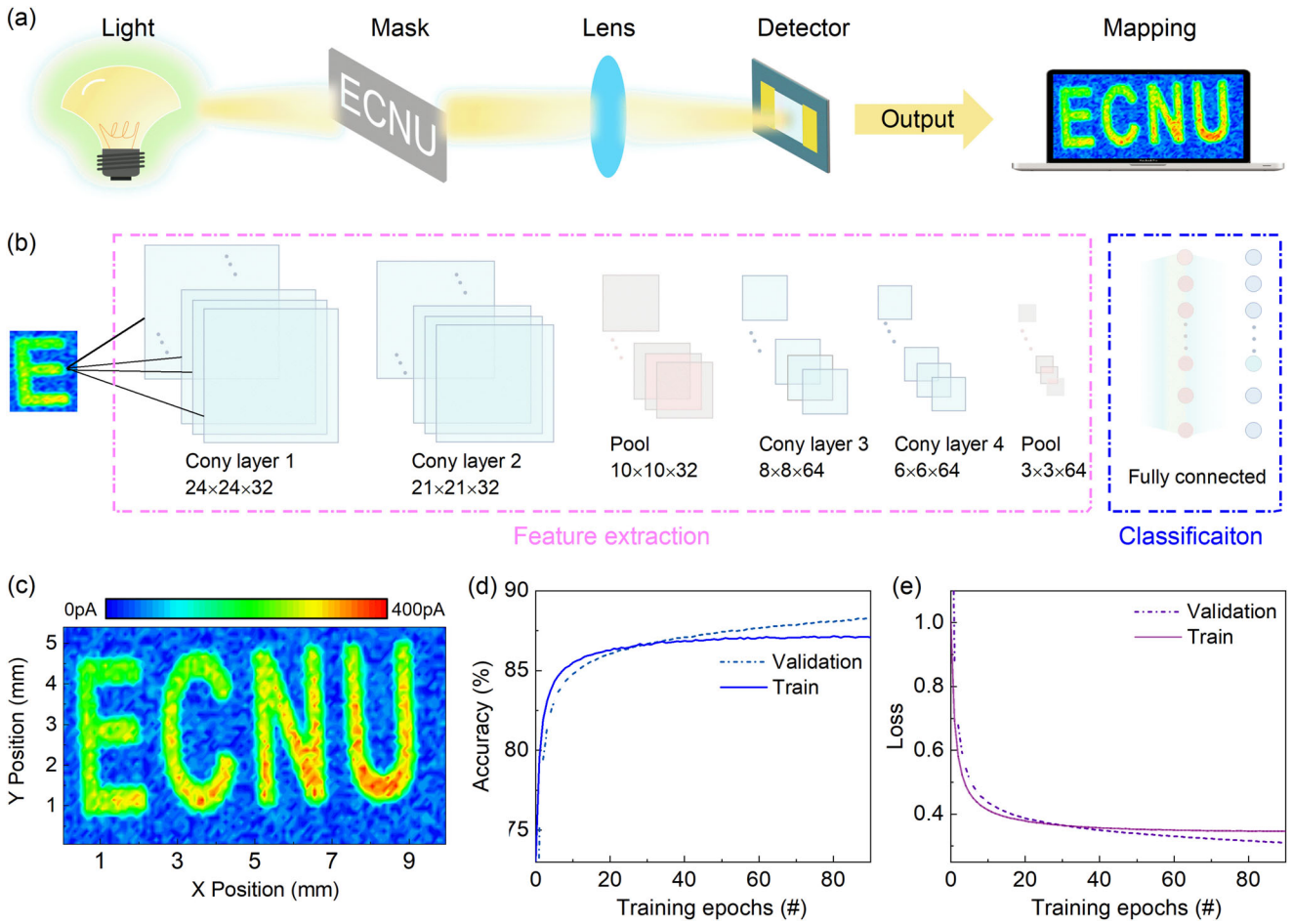

Figure 4. Room-temperature photodetector imaging and image recognition supported by CNN. a) Schematic diagram of the imaging measurement system based on the BP/MoS_2/CIPS-based photodetector. b) Schematic diagram of CNN for image recognition. c) The photocurrent imaging results of the pattern "ECNU" at V_{DS} = 0 V. Training and validation comparison of image recognition d) accuracy and e) loss.

larization reliability, the advantages of low power consumption, high speed, and flexible integration position ferroelectric polarization as a core pathway for constructing brain-inspired computing hardware. This approach holds promise for breakthroughs in applications such as visual perception.[44,45]

3. Conclusion

In conclusion, a BP/MoS_2/CIPS-based broadband photodetector has been developed and optimized by the polarization of ferroelectric CIPS. At the up state, the dark current of the photodetector is reduced by an order of magnitude, while the light detectivity is improved. Fortunately, the peak specific blackbody detection reaches 1.17×10^{10} cm · $Hz^{1/2}$ · W^{-1}. The method of optimizing device structure through 2D ferroelectric material polarization fields also lays the foundation for the future development of high-performance photodetectors. The CNN simulation performed at the system level shows a high image recognition accuracy under both ideal and experimental conditions. The BP/MoS_2/CIPS-based ferroelectric photodetectors have potential applications in next-generation image recognition.

4. Experimental Section

Device Fabrication and Characterization: The BP, MoS_2 and CIPS nanosheets were obtained by mechanical exfoliation in a glove box from the corresponding bulk crystals (Shanghai Onway Techology Co., Ltd) and then transferred and stacked through a dry transfer method to form a ferroelectric BP/MoS_2/CIPS heterostructure. The source and drain electrodes (15 nm/45 nm Cr/Au) were deposited by thermal evaporation using electron beam lithography (EBL). FEI Titan Themis 200F was used to reveal the morphology of the stepwise MoS_2 diode. Cross-sectional TEM (Thermo Fisher Scientific, Tecnai F20) and STEM (Thermo Fisher Scientific, Themis Z) were conducted to study the layered structure and interfaces of BP, MoS_2 and CIPS. Raman spectra (Jobin-Yvon LabRAM HR Evolution, Horiba) were characterized with a 532-nm excitation laser. The surface potentials of the device were measured by kelvin probe force microscopy system (KPFM Dimension Icon, Bruker).

Photoelectric Characterization: The electronic characteristics were measured by an Agilent B2902A source. A homemade wavelength-tuneable multichannel mid-infrared (MIR) light (2.5–4.2 μm) was used to study the MIR performance of the pho-

todetector. The diameter of the MIR beam was 3 mm. The laser, with a wavelength from 295 to 2000 nm, was focused on the device using a 100x objective lens. Blackbody tests were performed using a calibrated commercial blackbody furnace (HFY-206A). After the frequency was modulated by an optical chopper wheel, the photocurrent signal was converted into a voltage signal using a current preamplifier (Stanford Research Systems SR570) and recorded by a lock-in amplifier (Ametek Model 7270 DSP). The transient photocurrent response was recorded using an oscilloscope (Tektronix DPO 5204) to analyse the photoresponse time. All measurements were performed at room temperature in an ambient environment.

Supporting Information

Supporting Information is available from the Wiley Online Library or from the author.

Acknowledgements

This work was supported by the Strategic Priority Research Program of the Chinese Academy of Sciences (Grant No. XDB0580000); National Natural Science Foundation of China (Grant Nos. 62074058, 62327812, 62422410, 62361136587); Shanghai Rising Star Program (Grant No. 24QA2711000) and CAS Pioneer Hundred Talents Program; Open Fund of State Key Laboratory of Infrared Physics (Grant No. SITP-NLIST-YB-2024-02), International Research Center of Big Data for Sustainable Development Goals for providing us with data and East China Normal University Multifunctional Platform for Innovation (004); Natural Science Foundation of Henan (Grant No. 242300421693), the Key scientific research project plan of Henan Higher Education Institutions (Grant No. 24A430031), and the Interdisciplinary Sciences Project of Nanyang Institute of Technology (Grant No. 23NGJY002).

Conflict of Interest

The authors declare no conflict of interest.

Author Contributions

R.J. and Y.J. contributed equally to this work. R.J. and F.W. conceived the project and designed the experiments. R.J., Y.J., Z.Z., and F.D. fabricated devices. R.J., Y.J., Z.W., H.S., Y.S., and F.D. performed optical and electrical measurements. X.S. is responsible for letter recognition simulation. R.J., Y.J., J.Z., L.W., W.H., G.L., and Z.H. analyzed the data. R.J., Y.J., F.D., J.W., and F.W. co-wrote the manuscript. All authors have given approval to the final version of the manuscript.

Data Availability Statement

The data that support the findings of this study are available from the corresponding author upon reasonable request.

Keywords

broadband photodetector, convolutional neural networks, ferroelectric regulation, intelligent recognition, 2D materials

Received: February 10, 2025
Revised: April 21, 2025
Published online:

[1] T. Jin, J. Mao, J. Gao, C. Han, K. P. Loh, A. T. S. Wee, W. Chen, *ACS Nano* **2022**, *16*, 13595.
[2] L. Qi, S. Ruan, Y.-J. Zeng, *Adv. Mater.* **2021**, *33*, 2005098.
[3] S. Singh, K.-H. Kim, K. Jo, P. Musavigharavi, B. Kim, J. Zheng, N. Trainor, C. Chen, J. M. Redwing, E. A. Stach, R. H. Olsson, D. Jariwala, *ACS Nano* **2024**, *18*, 17958.
[4] W. Wang, Y. Zhang, W. Wang, M. Luo, Y. Meng, B. Li, Y. Yan, D. Yin, P. Xie, D. Li, D. Chen, Q. Quan, S. Yip, W. Hu, J. C. Ho, *Matter* **2024**, *7*, 2236.
[5] S. Sarkar, Z. Han, M. A. Ghani, N. Strkalj, J. H. Kim, Y. Wang, D. Jariwala, M. Chhowalla, *Nano Lett.* **2024**, *24*, 13232.
[6] F. Liu, L. You, K. L. Seyler, X. Li, P. Yu, J. Lin, X. Wang, J. Zhou, H. Wang, H. He, S. T. Pantelides, W. Zhou, P. Sharma, X. Xu, P. M. Ajayan, J. Wang, Z. Liu, *Nat. Commun.* **2016**, *7*, 12357.
[7] J. Zhou, A. Chen, Y. Zhang, D. Pu, B. Qiao, J. Hu, H. Li, S. Zhong, R. Zhao, F. Xue, Y. Xu, K. P. Loh, H. Wang, B. Yu, *Adv. Mater.* **2023**, *35*, 2302419.
[8] A. Dey, W. Yan, N. Balakrishnan, S. Xie, Z. R. Kudrynskyi, O. Makarovskiy, F. Yan, K. Wang, A. Patan, *2D Mater.* **2022**, *9*, 035003.
[9] W. Ci, P. Wang, W. Xue, H. Yuan, X. Xu, *Adv. Funct. Mater.* **2024**, *34*, 2316360.
[10] J. Cheng, P. Zhang, X. Ouyang, W. Tang, B. Song, Y. Zhang, Y. Zheng, A. Pan, *Adv. Funct. Mater.* **2024**, *34*, 2416333.
[11] J. Wu, J. Zhang, R. Jiang, H. Wu, S. Chen, X. Zhang, W. Wang, Y. Yu, Q. Fu, R. Lin, Y. Cui, T. Zhou, Z. Hu, D. Wan, X. Chen, W. Hu, H. Liu, J. Lu, Z. Ni, *Nat. Commun.* **2025**, *16*, 564.
[12] C. Tan, H. Wu, Z. Lin, L. Yang, Z. Wang, *Adv. Funct. Mater.* **2024**, *34*, 2415360.
[13] F. Wang, T. Zhang, R. Xie, Z. Wang, W. Hu, *Nat. Commun.* **2023**, *14*, 2224.
[14] L. Tong, Z. Peng, R. Lin, Z. Li, Y. Wang, X. Huang, K.-H. Xue, H. Xu, F. Liu, H. Xia, P. Wang, M. Xu, W. Xiong, W. Hu, J. Xu, X. Zhang, L. Ye, X. Miao, *Science* **2021**, *373*, 1353.
[15] Y. Chen, Y. Wang, Z. Wang, Y. Gu, Y. Ye, X. Chai, J. Ye, Y. Chen, R. Xie, Y. Zhou, Z. Hu, Q. Li, L. Zhang, F. Wang, P. Wang, J. Miao, J. Wang, X. Chen, W. Lu, P. Zhou, W. Hu, *Nat. Electron.* **2021**, *4*, 357.
[16] R. Rao, R. Selhorst, B. S. Conner, M. A. Susner, *Phys. Rev. Mater.* **2022**, *6*, 045001.
[17] R. Rao, B. S. Conner, R. Selhorst, M. A. Susner, *Phys. Rev. B* **2021**, *104*, 235421.
[18] F. Wang, X. Zou, M. Xu, H. Wang, H. Wang, H. Guo, J. Guo, P. Wang, M. Peng, Z. Wang, Y. Wang, J. Miao, F. Chen, J. Wang, X. Chen, A. Pan, C. Shan, L. Liao, W. Hu, *Adv. Sci.* **2021**, *8*, 2100569.
[19] Z. Zhou, J.-J. Zhang, G. F. Turner, S. A. Moggach, Y. Lekina, S. Morris, S. Wang, Y. Hu, Q. Li, J. Xue, Z. Feng, Q. Yan, Y. Weng, B. Xu, Y. Fang, Z. X. Shen, L. Fang, S. Dong, L. You, *Appl. Phys. Rev.* **2024**, *11*, 011414.
[20] Q. Xia, J. J. Yang, *Nat. Mater.* **2019**, *18*, 309.
[21] J. Chen, C. Zhu, G. Cao, H. Liu, R. Bian, J. Wang, C. Li, J. Chen, Q. Fu, Q. Liu, P. Meng, W. Li, F. Liu, Z. Liu, *Adv. Mater.* **2021**, *34*, 2104676.
[22] H. Zhu, J. Li, Q. Chen, W. Tang, X. Fan, F. Li, L. Li, *ACS Nano* **2023**, *17*, 1239.
[23] Y. Wu, N. T. Duong, Y. Chien, S. Liu, K. Ang, *Adv. Electron. Mater.* **2023**, *10*, 2300481.
[24] J. Wu, H.-Y. Chen, N. Yang, J. Cao, X. Yan, F. Liu, Q. Sun, X. Ling, J. Guo, H. Wang, *Nat. Electron.* **2020**, *3*, 466.
[25] E. Yang, K. R. Kim, J. Chang, *IEEE Electron Device Lett.* **2021**, *42*, 1472.
[26] X. Jiang, X. Zhang, R. Niu, Q. Ren, X. Chen, G. Du, Y. Chen, X. Wang, G. Tang, J. Lu, X. Wang, J. Hong, *Adv. Funct. Mater.* **2023**, *33*, 2213561.
[27] Y. Li, J. Fu, X. Mao, C. Chen, H. Liu, M. Gong, H. Zeng, *Nat. Commun.* **2021**, *12*, 5896.
[28] Y. Bai, W. Hao, Y. Wang, J. Tian, C. Wang, Y. Lei, Y. Yang, X. Yao, Q. Liu, C. Li, M. Gu, J. Wang, *PRX Energy* **2024**, *3*, 023004.

[29] M. Lanza, A. Sebastian, W. D. Lu, M. Le Gallo, M.-F. Chang, D. Akinwande, F. M. Puglisi, H. N. Alshareef, M. Liu, J. B. Roldan, *Science* **2022**, *376*, eabj9979.
[30] W. Cao, H. Bu, M. Vinet, M. Cao, S. Takagi, S. Hwang, T. Ghani, K. Banerjee, *Nature* **2023**, *620*, 501.
[31] D. Ielmini, H. S. P. Wong, *Nat. Electron.* **2018**, *1*, 333.
[32] F. Wang, W. Hu, *Nat. Mater.* **2023**, *22*, 1433.
[33] Z. Lin, Z. Tong, J. Zhang, F. Wang, T. Xu, Y. Zhao, X. Wu, C. Peng, W. Lu, Q. Zhao, J. Chen, *J. Semicond.* **2022**, *43*, 031401.
[34] L. You, Y. Zhang, S. Zhou, A. Chaturvedi, S. A. Morris, F. Liu, L. Chang, D. Ichinose, H. Funakubo, W. Hu, T. Wu, Z. Liu, S. Dong, J. Wang, *Sci. Adv.* **2019**, *5*, eaav3780.
[35] J. Bullock, M. Amani, J. Cho, Y.-Z. Chen, G. H. Ahn, V. Adinolfi, V. R. Shrestha, Y. Gao, K. B. Crozier, Y.-L. Chueh, A. Javey, *Nat. Photon.* **2018**, *12*, 601.
[36] M. Tamulewicz, J. Kutrowska-Girzycka, K. Gajewski, J. Serafińczuk, A. Sierakowski, J. Jadczak, L. Bryja, T. P. Gotszalk, *Nanotechnology* **2019**, *30*, 245708.
[37] X. Liu, D. Qu, H.-M. Li, I. Moon, F. Ahmed, C. Kim, M. Lee, Y. Choi, J. H. Cho, J. C. Hone, W. J. Yoo, *ACS Nano* **2017**, *11*, 9143.
[38] F. Dai, F. Wang, H. Ge, R. Xie, R. Jiang, H. Shi, H. Liu, G. Hu, L. Shen, T. Li, W. Hu, *IEEE Electron Device Lett.* **2024**, *45*, 16.
[39] F. Wang, F. Dai, Y. Li, H. Guo, *Infrared Phys. Technol.* **2022**, *125*, 104309.
[40] S. Du, W. Lu, A. Ali, P. Zhao, K. Shehzad, H. Guo, L. Ma, X. Liu, X. Pi, P. Wang, H. Fang, Z. Xu, C. Gao, Y. Dan, P. Tan, H. Wang, C. Lin, J. Yang, S. Dong, Z. Cheng, E. Li, W. Yin, J. Luo, B. Yu, T. Hasan, Y. Xu, W. Hu, X. Duan, *Adv. Mater.* **2017**, *29*, 1700463.
[41] M. Long, A. Gao, P. Wang, H. Xia, C. Ott, C. Pan, Y. Fu, E. Liu, X. Chen, W. Lu, T. Nilges, J. Xu, X. Wang, W. Hu, F. Miao, *Sci. Adv.* **2017**, *3*, e1700589.
[42] M. Long, Y. Wang, P. Wang, X. Zhou, H. Xia, C. Luo, S. Huang, G. Zhang, H. Yan, Z. Fan, X. Wu, X. Chen, W. Lu, W. Hu, *ACS Nano* **2019**, *13*, 2511.
[43] S. Tang, J. An, F. Song, M. Lv, K. Han, X. Peng, *ACS Appl. Mater. Interfaces* **2021**, *13*, 51414.
[44] X. Liu, K. Katti, D. Jariwala, *Matter* **2023**, *6*, 1348.
[45] C. Leblanc, S. Song, D. Jariwala, *Curr. Opin. Solid St. M.* **2024**, *32*, 101178.